JGR Solid Earth

RESEARCH ARTICLE
10.1029/2022JB024610

Brittle Creep and Failure: A Reformulation of the Wing Crack Model

Yves Bernabé[1] **and Matej Pec**[1]

[1]Department of Earth Atmospheric and Planetary Sciences, Massachusetts Institute of Technology, Cambridge, MA, USA

Key Points:

- Sliding cracks and their wing cracks interact with nearby flaws to form shear bands, which coalesce to form shear bands at greater scales
- Formation, growth, and coalescence of shear bands are self-similar over a range of length-scales and are expressed by a power law function
- Our model returns experimentally measurable quantities and reproduces trimodal creep curves and failure stresses obeying the Mohr-Coulomb criterion

Correspondence to:
M. Pec,
mpec@mit.edu

Citation:
Bernabé, Y., & Pec, M. (2022). Brittle creep and failure: A reformulation of the wing crack model. *Journal of Geophysical Research: Solid Earth*, *127*, e2022JB024610. https://doi.org/10.1029/2022JB024610

Received 19 APR 2022
Accepted 29 AUG 2022

Author Contributions:
Conceptualization: Yves Bernabé, Matej Pec
Formal analysis: Yves Bernabé
Funding acquisition: Matej Pec
Methodology: Yves Bernabé
Writing – original draft: Yves Bernabé
Writing – review & editing: Matej Pec

Abstract We propose a reformulation of the wing crack model of brittle creep and failure. Experimental studies suggest that the mechanical interactions of sliding and tensile wing cracks are complex, involving formation, growth, and coalescence of multiple tensile, shear and mixed-mode cracks. Inspired by studies of failure in granular media, we propose that these complex mechanical interactions lead to the formation of micro shear-bands, which, in turn, develop longer wing cracks and interact with a wider volume of rock to produce larger shear bands. This process is assumed to indefinitely continue at greater scales. We assume that the original wing crack formalism is applicable to micro shear-band formation, with the difference that the half-length, a, of the characteristic micro shear band is allowed to increase with wing crack growth. In this approach, the functional relationship of a with the wing crack length l embodies the entire process of shear band formation, growth and interaction with other shear bands and flaws. We found that the function $a(l)/a(0) = 1 + (l/\lambda)^q$, where λ and q are constant parameters, generated creep curves consistent with published creep data of rocks. Similar accord was also obtained with experimental brittle failure data. Furthermore, we found that the Mohr-Coulomb behavior emerged from our model, allowing estimation of the cohesion and angle of internal friction in materials for which λ and q are independently known.

Plain Language Summary Rocks close to Earth's surface deform by fracturing. Fracturing can occur abruptly if the load the rocks bear increases rapidly. Fracturing can however also occur over much longer times without changes to the load during a process called brittle creep. Observations suggest that fracturing occurs due to growth and linkage of many small-scale flaws present in the rock. The details of this growth and linkage process, however, are very complex which complicates our ability to assess when rocks will ultimately break. Here, we develop a model that simplifies the details of these small-scale interactions between large populations of flaws into a simple functional form. We analyze a number of possible functional forms and find that the simplest power law form yields good agreement with experimental data. Our model reproduces the behavior observed in brittle creep experiments, where after a step increase in load, the initially rapid rate of deformation first slows down, reaches a transitory steady-state and then accelerates until final failure occurs. Our model hence improves our ability to predict when failure will occur and presents a step toward mitigating the hazards associated with rock failure.

1. Introduction

Deformation in Earth's upper crust is dominated by fracturing and frictional sliding resulting in macroscopically "brittle" behavior. Fractures occur over a range of length scales from intragranular microscopic cracks to fault zones spanning plate boundaries that host destructive earthquakes. The stress in the upper crust is limited by frictional sliding on favorably oriented faults (e.g., Zoback & Zoback, 2007) and therefore much focus was dedicated to the problem of sliding frictional interfaces which are the end-product of brittle failure (e.g., Marone, 1998; Dieterich, 2007). Brittle creep and brittle failure that precede the formation of a throughgoing fault are relatively less studied phenomena, but nevertheless critical to our understanding of the long-term behavior of the crust and the earthquake cycle (e.g., Brantut et al., 2013; Main, 2000).

Macroscopic limit laws such as Mohr-Coulomb failure envelope and Byerlee's rule for frictional sliding are used to describe brittle deformation on the continuum scale and can be used to predict the strength of rocks and orientation of faults upon failure. Linking these empirical macroscopic failure laws to the underlying microscopic defects however remains elusive. Brittle deformation has been investigated from the point of view of micromechanics mostly using the idea that sliding, shear-loaded microcracks propagate out-of-plane as tensile cracks called wing cracks (Brace & Bombolakis, 1963; Horii & Nemat-Nasser, 1985). This concept has been incorpo-

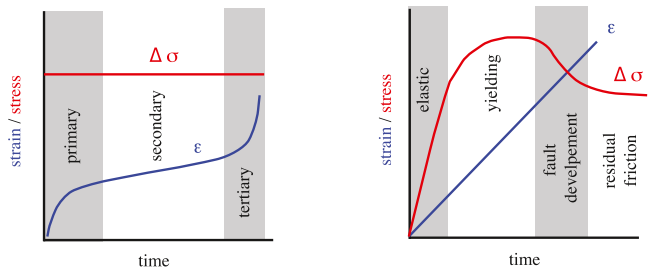

Figure 1. Schematic of typical curves of stress and strain versus time recorded in laboratory constant stress (left diagram) and constant strain rate tests (right diagram).

rated in models that take multiple crack interactions into account (Ashby & Hallam, 1986; Ashby & Sammis. 1990; Brantut et al., 2012). However, these models only consider very simplified crack interactions, by limiting the crack coalescence patterns to tensile merging of neighboring wing cracks. Our aim in the present paper is to construct an improved micromechanical model of brittle deformation that includes the complex crack interactions underlying the intricate coalescence patterns observed in laboratory studies such as Wong and Einstein (2009a, 2009b).

1.1. Background: The Wing Crack Model

In the laboratory, rocks are typically tested under either constant stress or constant strain rate boundary conditions (or more precisely under constant load or constant displacement rate boundary conditions). Typical stress-strain-time plots obtained for both types of tests are schematically illustrated in Figure 1. Under constant stress, rocks exhibit trimodal creep curves. Namely, decelerating "primary creep" occurs after the initial change in stress, followed by a transitory, apparent steady state "secondary creep," which eventually gives way to accelerating "tertiary creep" and failure (Figure 1, left diagram). In constant strain rate tests, rocks first deform elastically (albeit, often nonlinearly) until the yield point (i.e., onset of inelastic deformation), followed by strain hardening and accumulation of permanent strain. The axial stress eventually reaches a maximum (peak stress or strength), at which point a fault starts developing and the rock weakens to a stress level dictated by the residual friction on the fault (Figure 1, right diagram). This macroscopic behavior is controlled by the activation, propagation, and interactions of cracks in the rocks in the brittle regime. Loading conditions in nature are generally more complex than those employed in experiments, nevertheless laboratory tests can provide valuable insights into the micromechanics of brittle creep and brittle failure.

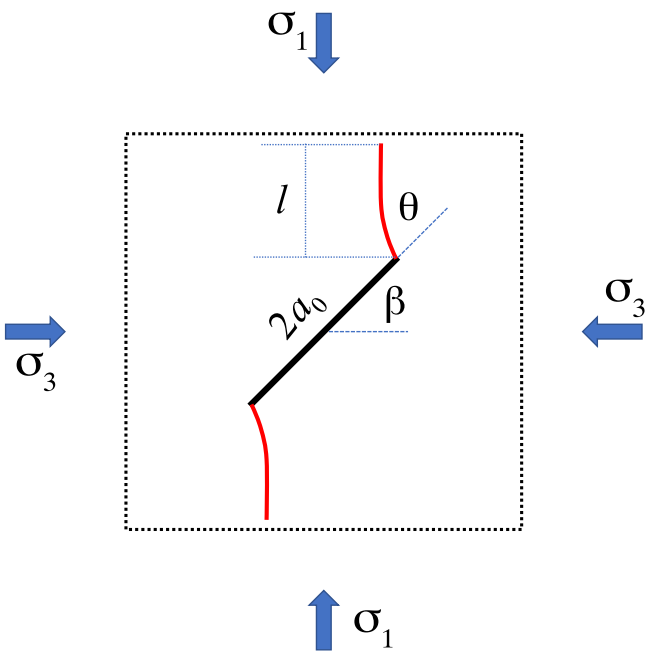

Figure 2. Schematic of a sliding microcrack and the associated wing cracks. The sliding crack is located in an infinite homogeneous solid subjected to compressive stresses. The intermediate stress σ_2 is normal to the figure plane. The angle β is, hereafter, assumed to be 45°.

The wing crack model, also called the sliding crack model, was proposed in the early 1960s to interpret the observations mentioned above, in particular the nearly ubiquitous development of tensile microcracks in crystalline rock samples subjected to compressive stresses (Brace & Bombolakis, 1963; see Paterson & Wong, 2005, for a review). The model attributes the rock inelastic deformation leading to failure to the formation of tensile cracks that emanate from the tips of the largest preexisting microcracks undergoing frictional shear. These activated microcracks are called the dominant cracks and are represented in the model by a single characteristic crack length, $2a_0$, and their inclinations with respect to the remotely applied principal compressive stresses, $\sigma_3 < \sigma_2 < \sigma_1$ (note that this inequality implies the geophysics convention of positive compressive stresses and strains, which will be used throughout the paper). Although cracks in rocks have a broad range of orientations, we follow the common practice of only considering the cracks for which the resolved shear stress is maximum (e.g., Baud et al., 2014) as the largest, most optimally oriented flaws will start propagating first. Thus, the model defines the dominant cracks as oriented parallel to the intermediate stress σ_2 and inclined with respect to the minimum stress σ_3 by an angle $\beta = 45°$ (Figure 2). The intermediate stress plays no role in the process of rock failure except for controlling the orientation of the final fracture. Although experimental observations have shown that brittle failure is indeed affected by the intermediate principal stress (Paterson & Wong, 2005), we will not attempt to modify this assumption in our model. A discussion of the effect of σ_2 is considered out of the scope of the present paper.

In the idealized conditions depicted in Figure 2, the wing cracks are curved. The angle θ they form with the dominant microcrack changes during propagation, starting at about 70° at initiation and decreasing until the wing cracks

become parallel to σ_1. Considering that the dominant cracks have the most effective orientation, $\beta = 45°$, the normal stress and the resolved shear stress on the sliding cracks are as follows:

$$\sigma_N = ½ (\sigma_1 + \sigma_3) \quad (1)$$

$$|\tau| = ½ (\sigma_1 - \sigma_3) \quad (2)$$

Part of the shear stress is balanced by friction. According to Amonton's law, the effectively active shear stress is therefore given by

$$|\tau_{\text{eff}}| = |\tau| - \mu\sigma_N, \quad (3)$$

where μ is the friction coefficient and the condition $|\tau| \geq \mu\sigma_N$ imposes $\sigma_1/\sigma_3 \geq (1 - \mu)/(1 + \mu)$.

The mode I stress intensity factor, κ_I, of a wing crack is a complex function of the remotely applied principal stresses, the length $2a_0$ of the dominant crack, the wing crack length l, and the angles β and θ (Figure 2). A number of models have been published (see Baud et al., 1996, for a review). Although they differ in some details depending on how the curvature of the wing cracks and other such features are treated, they all consist of the sum of two terms, one driving and one resisting wing crack propagation. Here, we consider the simple model from Kachanov (1982) (also used in Brantut et al., 2013)

$$\kappa_I = -1.15|\tau_{\text{eff}}|\sqrt{\pi a_0} + \sigma_3\sqrt{\pi l/2} \quad (4)$$

Although the Kachanov model ignores the wing crack curvature and, therefore, describes the early stage of wing crack development relatively poorly, it becomes quite accurate when the wing cracks become straight and fully aligned with the maximum principal stress (Brantut et al., 2013). The model predicts that wing cracks will form when the initial stress intensity factor is larger than the rock fracture toughness, $|\kappa_0| = 1.15|\tau_{\text{eff}}|\sqrt{\pi a_0} \geq |\kappa_{Ic}|$, or in other words, when $|\tau_{\text{eff}}|$ exceeds a critical shear stress $\tau_c = |\kappa_{Ic}|/\left(1.15\sqrt{\pi a_0}\right)$. The first (driving) term in Equation 4 expresses the wedging effect of shear displacements at the tips of the dominant crack. The second (resistant) term depends on l and accounts for wing crack closure caused by σ_3. The two terms have different signs, causing $|\kappa_I|$ to decrease with increasing l. Wing crack growth will therefore stop when κ_I becomes equal to κ_{Ic}, or in other words, when the wing crack length reaches $l_0 = 2a_0\,(1.15\,(|\tau_{\text{eff}}| - \tau_c)/\sigma_3)^2$.

This ultimate crack arrest means that the behavior of a single wing crack system cannot be used to model brittle failure except, perhaps, in uniaxial compression conditions (increasing σ_1 and $\sigma_3 = \sigma_2 = 0$), when the wing cracks eventually intersect the sample edges (i.e., axial splitting). But this difficulty can be resolved by recognizing that the rock contains a broad population of mechanically interacting flaws. Interacting dominant cracks are expected to experience an increase of $|\kappa_I|$ during wing crack extension. The currently published crack interaction models are all variations of the model developed by Ashby and Hallam (1986) and Ashby and Sammis (1990). The main idea of the model is that the dominant microcracks are spatially arranged in such a way that the wing cracks emanating from two neighboring sliding cracks are aligned and, owing to their mutual influence, the remotely applied lateral stress σ_3 is locally reduced in the ligaments between them by a quantity σ_i. This causes a decrease of the resistant term, $(\sigma_3 - \sigma_i)\sqrt{\pi l/2}$, and allows further propagation and finally coalescence of the wing cracks. The wing cracks thus form columns parallel to the maximum stress σ_1, which ultimately fail, owing to the classic buckling instability of slender columns. The intrinsic weakness of this model is the assumption of a very specific geometrical structure of the dominant microcracks, which is very unlikely to be found in a natural material. Nevertheless, the model has been quite successfully applied to experimental rock deformation and failure data (see the review by Brantut et al., 2013). Note also that these models are only concerned by dilatant deformation and therefore may not apply to highly porous rocks and/or very high confining pressure conditions (our model shares this limitation).

1.2. Background: Crack Coalescence

Since the early work of Horii and Nemat-Nasser (1985), the interaction and coalescence of wing cracks in conditions of uniaxial and biaxial compression have been experimentally investigated in a variety of materials, including rocks (see the comprehensive review of Wong, 2008). One important result is that biaxially loaded samples containing two parallel, cm-scale man-made crack-like flaws produced strongly different coalescence

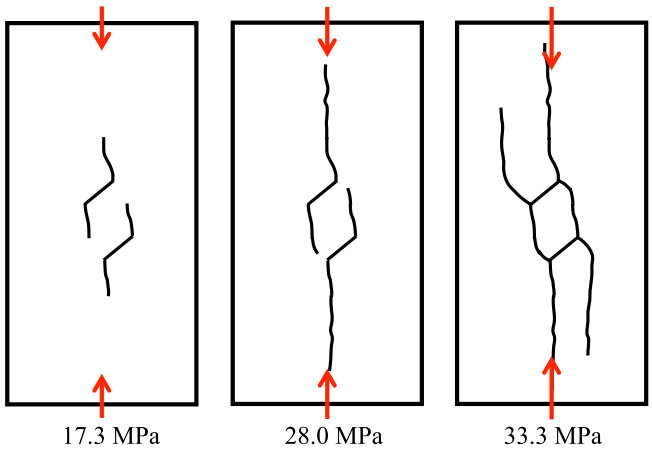

Figure 3. Simplified reproduction of Figure 12 of Lin et al. (2021). The boxes show the outlines of growing wing cracks at the surface of a mortar slab containing two cm-scale flaws. The slab was subjected to uniaxial compression in the direction of the red arrows (the values of the axial stress is indicated below each box). The initial flaws are positioned such that the wing cracks merge and new tensile cracks are produced from the other side of the sliding flaws.

patterns depending on their relative positions and inclinations with respect to the applied principal stresses (e.g., Wong & Einstein, 2009a, 2009b; Lin et al., 2021). In Lin et al. (2021), a scalar measure of the strain field was determined as a function of time using digital image correlation analysis, allowing identification of the fissures developing and coalescing around the initial flaws. In the configuration shown in Figure 3 (a schematic partial reproduction of Lin et al.'s (2021) Figure 12), the wing cracks emanating from the inclined flaws merged and two new ones were created on the sides, forming a column aligned with σ_1 quite similar to the structure assumed in the Ashby-Hallam-Sammis model. However, the unstable buckling of the column predicted in the Ashby-Hallam-Sammis model was not observed, perhaps because the experiment was prematurely stopped.

In other configurations of the initial flaws, very different coalescence patterns occurred, in which the inclined shear cracks themselves were actively involved. For example, a separate, small shear crack formed between two nearly aligned initial flaws and eventually merged with both of them, completely bridging the ligament (Figure 4). Very complex bridging structures combining tensile, shear and mixed mode cracks were also observed in other configurations of the initial flaws.

Similar coalescence patterns were produced in samples of Carrara marble and molded gypsum (Wong & Einstein, 2009a, 2009b). For example, nearly aligned flaws produced bridging shear cracks, while merging of the tensile wing cracks occurred when the flaws were shifted to form a 90° angle. Combinations of shear, tensile and mixed mode bridging cracks were observed in other cases.

2. The Model

2.1. The Concept: Micro to Macroscopic Shear Bands

Despite the general similarity of the results described above, important differences were noted in materials with distinct internal structures. For example, development of a secondary crack was usually preceded in Carrara marble by an increase in light reflectivity (whitening) of the sample surface in a thin region exactly delineating the path of the future secondary crack (Wong, 2008; Wong & Einstein, 2009a, 2009b). These "white patches" visible on the sample surface prior to cracking can be attributed to the formation and accumulation of damage in highly strained thin zones. This explanation implies the existence, in the material, of a population of very small defects and microcracks (invisible to the eye or even a very high-resolution camera) that are activated by the amplified stresses around the large cm-scale flaws. White patches were not observed in molded gypsum, a microgranular material that was fabricated using procedures specifically designed to ensure excellent homogeneity. Lajtai (1974) similarly noticed the formation and growth of damaged shear zones at the tips of a sheared cm-scale synthetic crack in a biaxially stressed plaster slab. Evidence of interaction of large propagating cracks with smaller flaws is also reported in Brantut et al. (2014). Their Figure 12 shows examples of, on one hand, very smooth and rectilinear wing cracks in homogeneous sparitic calcite cement and, on the other, rough and tortuous cracks traversing microgranular micritic aggregations.

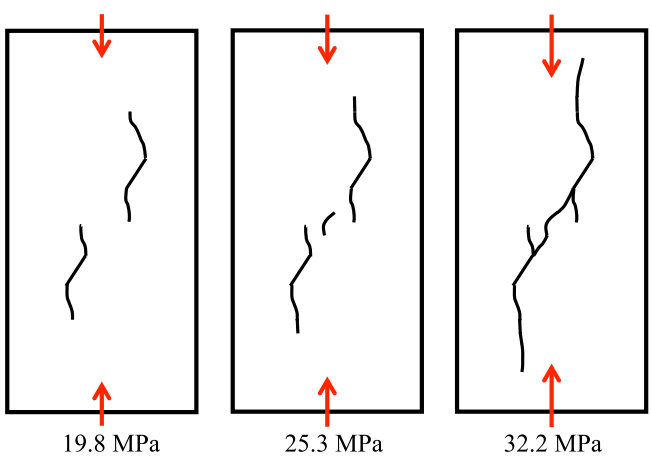

Figure 4. Simplified reproduction of Figure 7 of Lin et al. (2021). Here, the position of the initial flaws leads to the formation of a shear crack and the eventual bridging of the ligament between the initial flaws.

Shear failure also occurs in unconsolidated granular media (e.g., Desrues, 1990). At stresses below grain crushing stresses strain localization is observed on shear bands, which form by grain sliding and rotation. The initiation and growth of shear bands in granular materials has been extensively investigated experimentally and numerically (see Desrues, 1990, and references therein). One important observation is that the first stage of strain localization consists in the formation of multiple, separate micro shear

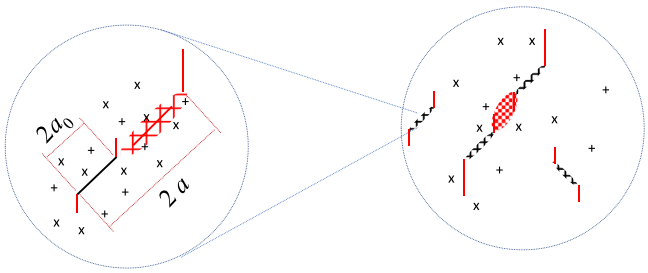

Figure 5. Schematic representation of mechanical interactions of cracks and flaws and the resulting micro shear band formation. The change of scale shown here is assumed to continuously take place at greater and greater scales.

bands. With increasing stress, some of these micro shear bands interact with neighboring ones, coalesce and eventually develop into macroscopic shear bands (Desrues & Andó, 2015). Similar scale increase scenarios have been observed in rocks. For example, Figure 16 in Brantut et al. (2013) shows the hypocenter locations of acoustic emissions recorded during a creep test of a granite sample. The distribution of hypocenters is random and featureless during primary and secondary creep but becomes concentrated into growing clusters during tertiary creep, eventually forming a single shear fracture (see also, Fortin et al., 2009, 2010; Lockner, 1993, 1998; Lockner et al., 1992). Here, we follow a similar concept. Natural flaws and microcracks in rocks have a very broad distribution of sizes. The (largest and most favorably oriented) dominant cracks are the first to develop wing cracks, which, as discussed above, are bound to interact with nearby minor flaws. We posit that this process will generally result in the development, near the tip of the dominant crack, of a complex array of microcracks (formed in tensile, shear and mixed mode) that globally deforms in shear. For lack of a better term, we will use the granular material terminology and call these structures micro shear bands. We emphasize that this term is meant to cover a broad range of damage structures, from simple merged shear cracks to inclined zones of crushed material. All these structures share a greater susceptibility to deform in shear than their surroundings, hence our choice to refer to them as shear bands. Shear cracks and micro shear bands similarly slide when submitted to sufficient shear stresses, although they may have different effective coefficients of friction. A wing crack should therefore develop at the outer edge of the shear band (Figure 5). Note that wing cracks have indeed been observed to initiate from the edges of sheared microstructural objects other than microcracks. For example, Rawling et al. (2002) present scanning electron microscope (SEM) images of wing cracks emanating from the edges of sheared biotite grains in triaxially deformed samples of Four-mile gneiss (e.g., see their Figure 9). Furthermore, owing to the overall increase in length, the wing crack emanating from a micro shear band will be longer than the initial one, and thus, have the capacity to interact with a greater volume of rock. It becomes therefore likely that two micro shear bands in favorable positions and orientations will coalesce to form even longer micro shear bands, from the edges of which increasingly long wing cracks will grow (Figure 5). The model does not include an upper cut-off scale and the process is therefore assumed to continue at indefinitely increasing scales.

2.2. Micro Shear Band Model: Brittle Failure

We posit that the brittle deformation of rock illustrated in Figure 5 can be described as the result of crack growth and coalescence around a representative dominant (or leading) micro shear band. Given the mechanical similarity of shear bands and sheared cracks, it is reasonable to assume that a leading micro shear band can be also modeled using the mathematical development rooted in linear elastic fracture mechanics leading to Equation 4, the only difference being that the half-length a of the leading micro shear band increases during loading.

Since the second term of Equation 4 describes the restraining effect of σ_3 on wing crack expansion, it does not need to be modified. In the first term, the friction coefficient entering the definition of τ_{eff} may depend on the internal structure of the shear band and thus vary during crack growth. For the sake of simplicity, we will assume that the friction coefficient of the micro shear bands remains approximately equal to that of the sheared cracks. Equation 4 then becomes

$$\kappa_I = -1.15|\tau_{\text{eff}}|\sqrt{\pi a(l)} + \sigma_3\sqrt{\pi l/2} \tag{5}$$

where the half-length of the micro shear band is an increasing function of l, $a(l)$, which provides a simple (albeit inexplicit) way to express the complex crack interactions leading to the formation of micro shear bands. Note that, in this model, wing crack growth causes an increase of the driving term $\sqrt{\pi a(l)}$ in Equation 5 instead of a reduction of the resistant term $\sigma_3\sqrt{\pi l/2}$ as in the Ashby-Hallam-Sammis model. Furthermore, we expect shear failure to naturally arise from the formation of increasingly long shear bands, whereas unstable buckling of axial columns has to be additionally invoked in the Ashby-Hallam-Sammis model.

If we assume that wing crack growth is stable (as it has to be when the mechanical interactions are negligible) the crack arrest condition, $\kappa_I = \kappa_{Ic}$, yields:

$$-1.15\,(|\tau_{\text{eff}}| - \tau_c)\,\sqrt{\pi a(l)} + \sigma_3\sqrt{\pi l/2} = 0 \tag{6}$$

If $|\tau_{\text{eff}}|$ is considered the independent variable (i.e., in constant loading rate tests), solving Equation 6 for $a(l)$ yields

$$a(l) = \frac{l}{2}(\sigma_3/1.15\,(|\tau_{\text{eff}}| - \tau_c))^2 \tag{7}$$

which simply states that $a(l)$ can be calculated if the dependence of l on $|\tau_{\text{eff}}|$ is known. In this description, failure occurs with increasing $|\tau_{\text{eff}}|$ when the leading shear band eventually reaches the sample boundaries. Rock failure tests, however, are usually carried out in constant strain rate conditions and not at constant loading rate as assumed by Equation 7. In this case, l is the independent variable and prior knowledge of $a(l)$ is needed to model brittle failure.

2.3. Micro Shear Band Model: Brittle Creep

Following previous models of brittle creep, we introduce time dependence by assuming subcritical crack growth. In this case, wing crack propagation can proceed at constant stresses below the critical shear stress τ_c. The initial stress intensity factor is $|\kappa_0| = 1.15|\tau_{\text{eff}}|\sqrt{\pi a_0} < |\kappa_{Ic}|$ and Equation 5 can be recast as

$$\frac{\kappa_I}{\kappa_0} = \sqrt{a(l)/a_0} - \frac{\sigma_3}{\kappa_0}\sqrt{\pi l/2} \tag{8}$$

Equation 8 can be further simplified by using the following dimensionless variables and parameters: $K_I = \kappa_I/\kappa_0$, $A = a/a_0$, and $L = l/l_0$, where $l_0 = 2a_0\,(1.15\,|\tau_{\text{eff}}|/\sigma_3)^2 = 2{\kappa_0}^2/(\pi{\sigma_3}^2)$, that is, the maximum possible length of the wing cracks generated under the current state of stress at the tips of a microcrack of length $2a_0$ in the absence of any mechanical interactions (l_0 is thus an intrinsic property of the dominant microcracks of the undeformed rock). Note that l_0 can be physically achieved when subcritical crack growth is operating since $|\kappa_I|$ is allowed to drop to zero. We finally obtain

$$\mathrm{K}_I = \sqrt{A(L)} - \sqrt{L} \tag{9}$$

Although Equation 9 is not a mechanistic model of crack coalescence, the function $A(L)$ is effectively a closed-form expression of the results of the extremely complex and varied mechanical interactions underlying the formation and growth of micro shear bands. To do the job correctly, $A(L)$ must satisfy a number of constraints. First, there are the trivial conditions that $A(0) = 1$ and $A(L)$ must be a monotonically increasing function. Thus, $A(L)$ can be expressed as $A(L) = 1 + f(L)$, where $f(L)$ is a monotonically increasing function verifying $f(0) = 0$. Most importantly, K_I must always be strictly larger than zero. Negative values obviously contradict the definition of K_I since κ_I and κ_0 are both negative quantities. Moreover, $K_I = 0$ implies crack arrest and is therefore incompatible with tertiary creep.

The simplest functions satisfying these conditions are the power law functions, $f(L) = (L/\Lambda)^q$, where $\Lambda = \lambda/l_0$ is a dimensionless length scale representing the normalized distance that the wing crack must propagate to enter the vicinity of another microcrack or flaw, interact with it and therefore produce a substantial increase of K_I. Of course, other more complex functions such as the polynomials, $f(L) = \sum_{i=1}^{q} C_i L^i$(with $C_i \geq 0$), can also meet the conditions above. We will focus here on the power laws $f(L) = (L/\Lambda)^q$, because they are the analytically simplest functions, and as will be discussed later, produced results in good agreement with experimental brittle creep data. We nevertheless investigated the polynomials $f(L) = (1 + L/\Lambda)^q - 1$ (i.e., $A(L) = (1 + L/\Lambda)^q$) as thoroughly as $f(L) = (L/\Lambda)^q$ but the results obtained were inconsistent with experimental brittle creep observations and will not be discussed in detail in the following text.

To illustrate how Equation 9 works, it is convenient to consider the perfect square function $A(L) = (1 + L/\Lambda)^2$ (see Figure 6). Since the square root of $A(L)$ is a linear function of L, the first term in Equation 9 yields a family of straight lines with slopes increasing when Λ is decreased (the values of Λ are indicated in the same color as the corresponding lines in Figure 6). The values of K_I are graphically measured as the vertical distance between

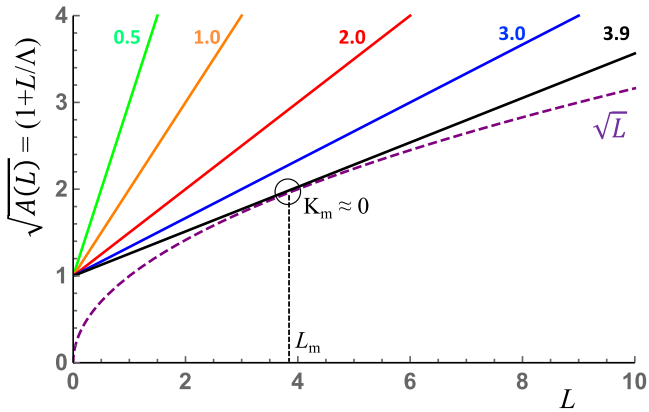

Figure 6. Graphic representation of Equation 9 in the case of $A(L) = (1 + L/\Lambda)^2$. The vertical distance between the colored straight lines (the values of Λ for each line are indicated in matching colors) and the dashed purple curve is a measure of the stress intensity factor K_I. The position L_m of the minimum stress intensity factor K_m of the black curve is indicated by the small empty circle and the associated vertical dashed line. Note that K_m is nearly equal to zero in this case. See text for a detailed interpretation.

these lines and the $\sqrt{L}$ curve representing the second term of Equation 9 (the dashed line in Figure 6). Thus, in all cases, K_I first decreases (primary creep), reaches a minimum (secondary creep), and then increases indefinitely (tertiary creep). To satisfy the condition, $K_I > 0$, the colored straight lines in Figure 6 are not allowed to intersect or tangentially touch the $\sqrt{L}$ curve, thus limiting the values that Λ can take (in this example, $\Lambda < \Lambda_c = 4$). We also note that increasing Λ causes a reduction of the minimum K_m of K_I and of the rate of increase of K_I in the second stage while the value L_m of L at the minimum increases (Figure 6). K_m and L_m are key output parameters of the model since they identify the transition from primary to tertiary creep.

The consecutive K_I-decreasing and K_I-increasing stages illustrated in Figure 6 were produced by the power laws $f(L) = (L/\Lambda)^q$ with an exponent $q \geq 2$ as well as all other functions $f(L)$ examined in this study. These various $f(L)$ functions, however, differed in the values of Λ_c, K_m, and L_m that they generated.

To assess the effect of the power law exponent q, we examined the form of the curves of K_I versus L associated with $f(L) = (L/\Lambda)^q$ for different values of q and Λ (the curves associated to $q = 2$ to 6 and $\Lambda = 1$ are shown in Figure 7).

The limit Λ_c is analytically related to the exponent q through the expression, $\Lambda_c = (q^{1/(1-q)} - q^{q/(1-q)})^{(1-q)/q}$ (see Appendix A for the derivation). According to this relation, Λ_c decreases from 2 to ~1.46 when q is increased from 2 to 8. As mentioned earlier, $\Lambda = \lambda/l_0$ represents the normalized distance, over which a wing crack must propagate to enter the vicinity of other microcracks and flaws and interact with them. It is important to note that this interaction distance depends both on the properties of the material being modeled and the state of stress considered. Indeed, the effect of the stress state is introduced through the normalization factor $l_0 \propto (|\tau_{eff}|/\sigma_3)^2$ while the material is described by both l_0, which contains a_0, and λ, which can be understood as a characteristic flaw separation (or the inverse of the flaw density). Consequently, variations of Λ may represent either distinct materials with differing flaw densities or a single material subjected to various levels of stress. Thus, an increase of q indicates an increase of either the flaw density of the rock considered or the level of stress needed to allow brittle creep. We also note that the minimum stress intensity factor K_m along the K_I versus L curves decreased with increasing q while the corresponding L_m first decreased and then increased (Figure 7).

Time dependence is then introduced in the model by assuming subcritical crack growth. According to this assumption, crack propagation proceeds gradually, starting at a stress intensity factor κ_0 lower than κ_{IC}. Although different subcritical crack growth models can be used, the most commonly reported in previous studies is based on the power law relation often called Charles' law (Charles, 1958; see also Wiederhorn & Bolz, 1970):

$$\frac{v}{v_0} = \left(\frac{\kappa_I}{\kappa_0}\right)^n \tag{10}$$

where v and v_0 are the current and initial growth rates of the wing cracks, and the exponent n usually takes very high values (between 10 and 50). Note that Equation 10 is dimensionless and can be re-written $V = K_I^n$, with $V = v/v_0$, and then combined with Equation 9 to yield:

$$V = \frac{dL}{dT} = \left(\sqrt{1 + f(L)} - \sqrt{L}\right)^n \tag{11}$$

where the normalized time is defined as $T = t/t_0 = tv_0/l_0$. Using the previously discussed functions $f(L) = (L/\Lambda)^q$, Equation 11 contains three parameters, the normalized flaw separation Λ, the power law exponent q, and the subcritical crack growth exponent n. Since L is a strictly monotonic, increasing function of T, Equation 11 can be numerically solved using the following simple

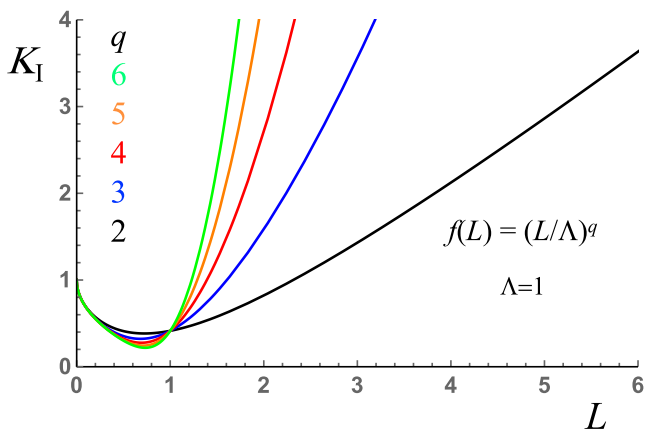

Figure 7. Examples of curves of stress intensity factor K_I versus wing crack length L associated with $f(L) = (L/\Lambda)^q$ with $\Lambda = 1$ for various values of the exponent q as indicated in matching colors. See text for a detailed discussion.

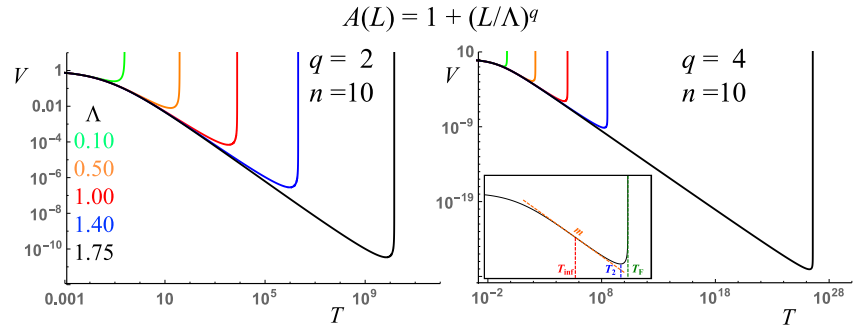

Figure 8. Examples of curves of wing crack growth rate V versus time T associated with $f(L) = (L/\Lambda)^q$ for $q = 2$ (left diagram) and 4 (right diagram). The values of Λ corresponding to each curve are indicated in matching colors (the subcritical crack growth exponent n was equal to 10 in all cases). The times T_{inf}, T_2, and T_F, and the exponent m are graphically defined in the inset. See text for a detailed discussion.

procedure. First we construct a wing crack length series, $L_i = (i - 1)\, dL$, where dL denotes a small increment (e.g., $dL = 0.01$ or lower for more accuracy). We then use Equation 10 to calculate the corresponding wing crack velocity series V_i. Finally, the time series T_i can be calculated using the recurrence $T_{i+1} = T_i + dT_i$, with dT_i calculated by numerical integration of $dT_i = \int_{L_i}^{L_{i+1}} \left(\sqrt{1 + f(L)} - \sqrt{L}\right)^{-n} dL$. Examples of curves of V as a function of T corresponding to $f(L) = (L/\Lambda)^q$ with $\Lambda = 0.1$, 0.5, 1.0, 1.4, and 1.75; $q = 2$ and 4; and $n = 10$ are shown in Figure 8.

In all cases considered in this study, the V versus L curves displayed the same generic shape consistent with the three classic stages of creep. As illustrated in Figure 8, the crack propagation velocity V first decreases gradually (decelerating or primary creep stage) down to a minimum value (secondary creep) and then sharply increases up to failure (accelerating or tertiary creep stage). The failure time T_F is obtained by integrating $dT = dL/V$ for L increasing from 0 to infinity.

$$T_F = \int_0^{\infty} \left(\sqrt{1 + f(L)} - \sqrt{L}\right)^{-n} dL \tag{12}$$

The integral of Equation 12 is convergent for all values of Λ satisfying condition $\Lambda < \Lambda_c$ and all functions $f(L)$ mentioned in previous sections. Figure 8 also shows that the decelerating stage consists of two segments, first the deceleration magnitude $|dV/dT|$ increases and then, after an inflection point is passed, decreases down to zero (i.e., the point where the accelerating stage begins). Comparison of the right- and left-hand diagrams demonstrates that increasing the polynomial degree q (for a given Λ) brings the minimum propagation velocity closer to zero, increases greatly the time to failure and strongly sharpens the transition to tertiary creep. Similar effects are produced by raising the subcritical crack growth exponent n (not shown in Figure 8).

Based on the results described above, three key points can be identified along the curve of V versus T, namely, (a) the inflection point within the decelerating creep stage, (b) the minimum of the curve (note that this point is the limit between the primary and tertiary creep segments; it can therefore be interpreted as the center of a secondary creep segment), and (c) the failure point. These three points are distinguished by their respective time coordinates, T_{inf}, T_2, and T_F (see inset in Figure 8). Furthermore, in a log-log plot, the tangent at the inflection point T_{inf} defines a local power law $V \propto T^{-m}$, which becomes steeper with increasing Λ (see inset in Figure 8). Although the individual normalized times T_2 and T_F may be difficult to determine experimentally because the time normalization, $T = t\, l_0/V_0$, involves l_0, a quantity that may not be experimentally accessible, the ratio T_F/T_2 is independent of normalization and can be measured in laboratory tests.

We measured T_F/T_2 for $f(L) = (L/\Lambda)^q$ in various conditions of Λ, q, and n. We observed that T_F/T_2 strongly decreased with increasing Λ when q was equal to 2, changed to a much flatter, non-monotonic behavior with increasing q from 3 to 5, and eventually became a steadily but moderately increasing function of Λ for $q = 6$ (Figure 9, right diagram). In all cases, T_F/T_2 approached a limit value of 2 for the largest Λ's while a wide range, from as high as 3 to as low as 1.6, was obtained for Λ near zero depending on the polynomial degree q.

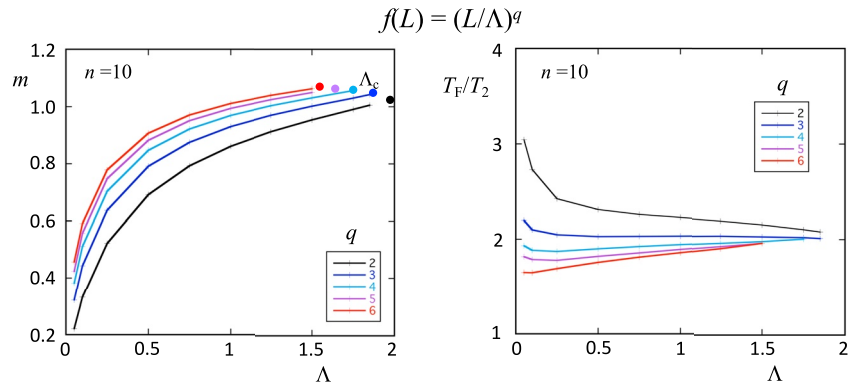

Figure 9. Examples of the predicted dependence of the primary creep exponent m (left diagram) and the failure time to secondary creep time ratio T_F/T_2 (right diagram) on the characteristic flaw separation Λ. These curves correspond to the function $f(L) = (L/\Lambda)^q$ with values of q indicated in matching colors (the subcritical crack growth exponent n was equal to 10 in all cases). The positions of the limit Λ_c for the different exponents q are indicated by colored solid dots in the left diagram. See text for a detailed discussion.

Because inflection points are patently difficult to determine from noisy data, T_{inf} is not a practical parameter to use for comparison with experimental data, but the exponent m is independent of time normalization and can be estimated as a characteristic power law exponent of rock primary creep data. We calculated m for a variety of values of Λ and q. We observed that m showed approximately logarithmic dependence on Λ for different values of q (Figure 9, left diagram). The calculated m's increased from values between 0.2 and 0.5, depending on q, at low Λ's to an upper limit of about 1 at Λ's approaching Λ_c (Figure 9, left diagram).

3. Discussion

3.1. Comparison With Experimental Data: Brittle Creep

Testing this model against experimental data cannot be done directly since the essential wing crack parameters l and v cannot be measured in rock samples during deformation. Even, estimating the half-length a_0 of the dominant flaws from SEM images of the undeformed rock is an extremely difficult and uncertain undertaking. We will assume here that the macroscopic creep strain rate $\dot{\varepsilon}$ of a very large volume of material containing many dominant microcracks is linearly related to the wing crack propagation velocity v. Note that the (usually nonlinear) relations between v and $\dot{\varepsilon}$ derived in various versions of the Ashby-Hallam-Sammis model (e.g., Brantut et al., 2012) cannot be used in our model. Indeed, these relations only include the effect of wing cracks growth and neglect the shear displacements along the dominant microcracks.

In our model, on the other hand, the macroscopic creep strain rate is mainly produced by formation and shearing of the micro shear bands. Accordingly, the experimental equivalent of the wing crack length l is the (inelastic) creep strain ε. Note that there is no measurable equivalent of l_0, making it impossible to normalize experimental time so that it can be directly compared to the model dimensionless time $T = t\, v_0/l_0$. However, the main output parameters of the model, the exponent m and the ratio t_F/t_2 can be estimated from experimental creep curves spanning the three regimes from primary to tertiary creep without time normalization. Note that experimental data are necessarily afflicted by noise, mostly random fluctuations of the readings of the measuring devices but sometimes also errors caused by computer glitches. Published data sometimes contain "unphysical" features in the recorded signals, like sharp steps (i.e., points of extremely high strain rates) or oscillations (i.e., alternating positive and negative strain rates), which require specific removal treatments (the easiest being manually passing a smooth curve through the steps or oscillations). Since the combination of regularization techniques needed for the purpose of differentiating the experimental ε versus t data strongly depended on the particular data being analyzed, we did not attempt to develop a comprehensive data-treatment workflow. Each data set was individually processed, although we made every effort to maintain consistency.

We downloaded or digitized the published brittle creep data of Inada granite (Fujii et al., 1999), Thala limestone (Brantut et al., 2013), Etna basalt (hereafter labeled Etna basalt 1; Heap, 2009; Heap et al., 2011), and Darley Dale

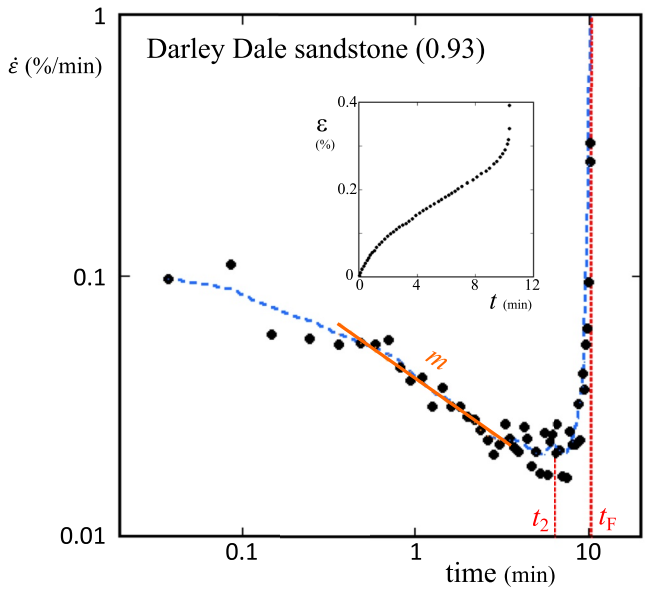

Figure 10. Example of a strain rate versus time curve calculated from a digitized experimental creep curve (here, a Darley Dale sandstone creep test at a creep to peak stress ratio of 0.93; Heap, 2009; Heap et al., 2009). Experimental data with (dotted blue line) and without smoothing (solid black dots) are shown. The digitized creep curve is displayed in the inset. The estimates of t_F, t_2, and the primary creep exponent m are graphically indicated. See text for a detailed discussion.

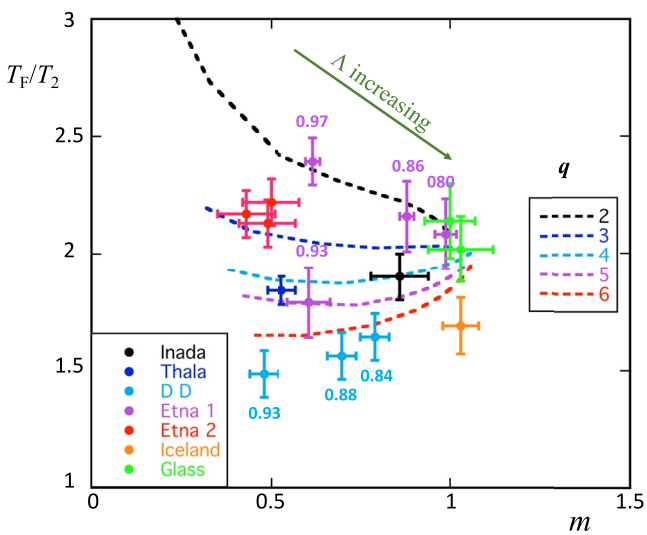

Figure 11. Experimental estimates of t_F/t_2 and m for Inada granite (black), Thala limestone (dark blue), Darley Dale sandstone (light blue), Etna basalt 1 (purple), Etna basalt 2 (red), Iceland basalt (orange), and thermally cracked glass (green). The error bars indicate the estimated uncertainties of the calculated values of t_F/t_2 and m. In the case of Darley Dale sandstone and Etna basalt 1, the creep stress levels (σ_1/σ_{peak}) are shown above the data points in matching color. The theoretical curves of T_F/T_2 versus m for the function $f(L) = (L/\Lambda)^q$ and various values of the exponent q as indicated in the inset on the right side of the diagram, are superposed on the experimental data. The olive green arrow indicates the direction in which the theoretical interaction distance Λ increases in this diagram.

sandstone (Heap, 2009; Heap et al., 2009) and calculated the corresponding time-dependent strain rates (simple differencing was used). In the case of Darley Dale sandstone and Etna basalt 1 (Heap, 2009), preliminary constant strain rate tests at different effective confining pressures were performed to determine the rock strength defined as the peak effective differential stress $\sigma_{peak} - \sigma_3$ (note that all stresses reported in the above references are effective stresses, i.e., differences of the total stresses and pore pressures). Creep tests at the same effective confining pressure (30 MPa) and various effective differential stresses $\sigma_1 - \sigma_3$ below the previously measured peak stresses were then carried out in samples from the same quarry blocks (Heap, 2009). These tests are particularly interesting to us since the samples had presumably identical properties and microstructures but were subjected to different stresses. We therefore expected that the experimental data would yield values of T_F/T_2 and m consistent with a single value of q and decreasing Λ's with increasing creep stress. We also analyzed creep curves measured in basalt samples from a different outcrop on Mount Etna (hereafter labeled Etna basalt 2, Mansbach, 2022) and a cored well in Iceland (Xing et al., 2022), and in thermally cracked glass cylinders (Mallet et al., 2014, 2015).

The experimental curves of $\log(\dot{\varepsilon})$ versus $\log(t)$ of these rock samples (e.g., Figure 10) appear indeed similar to the theoretical curves of Figure 8. We were, therefore, able to estimate the two primary output parameters, t_F/t_2 and m, from these data. The time to failure t_F is easy to measure but t_2 can be more challenging (note that superposing the smoothed creep curves and the original noisy ones is quite helpful to avoid unreasonable under- or over-estimations of t_2 and to estimate uncertainties). The inflection point within the decelerating stage is all but impossible to identify, but the power law exponent m can still be estimated by selecting a segment of data points at the center of the primary creep stage (see the example of Figure 10; again superposing the smoothed and original data is a very useful precaution). Within the estimated uncertainties, the measured values of the ratio t_F/t_2 ranged from about 1.5 to 2.2, and m from 0.4 to slightly over 1.

For comparison purposes, we superposed the experimental (m, t_F/t_2) data on the theoretical T_F/T_2 versus m curves obtained by cross-plotting the numerical results for the function $f(L) = (L/\Lambda)^q$ and constant values of q. Note that the theoretical curves converge from the left border to the vicinity of the point ($m = 1$; $T_F/T_2 = 2$), thus delimiting a wedge-shaped region that excludes values of m significantly exceeding one. The experimental results are in good agreement with the model in the sense that the measured data points approximately fall within the allowed wedge-shaped region (Figure 11). This observation also lends support to our assumption that the strain rate $\dot{\varepsilon}$ is linearly related to the wing crack propagation velocity v. Indeed, let us assume instead that $\dot{\varepsilon}$ is an arbitrary (monotonically increasing) function g of v. The experimental strain rate versus time curves (e.g., Figure 10) should then be compared to curves of $g(V)$ versus T, which should have similar shapes to the curves shown in Figure 8 but yield very different values of m. These changes would likely produce a very different Figure 11. They could significantly distort the region in (m; T_F/T_2) space allowed by the model and thus reduce or even destroy any agreement of model and experiments.

Although we cannot exclude that other functions besides $(L/\Lambda)^q$ may yield similarly satisfactory results, we can definitely eliminate the function $A(L) = (1 + L/\Lambda)^q$ (or $f(L) = (1 + L/\Lambda)^q - 1$), which only generated values of T_F/T_2 greater than 2 that are not consistent with more than half

the experimental data. We surmise that the unfitness of the function $A(L) = (1 + L/\Lambda)^q$ is shared by all polynomial functions combining terms of widely variable degrees in L/Λ, including linear and quadratic terms, which produce values of T_F/T_2 significantly greater than 2. If this is true, we can, hereafter, safely limit our discussion to the simple power laws $f(L) = (L/\Lambda)^q$.

If the functions $f(L) = (L/\Lambda)^q$ are indeed the appropriate functions for interpreting rock data, we can infer the values of q and Λ corresponding to each creep experiment. For example, $q \approx 4$ fits both Inada granite and Thala limestone although a larger Λ is associated to the granite than the limestone ($\Lambda \approx 0.5$ and 0.1, respectively). It is tempting to interpret this result as indicating that the granite, whose low porosity (0.45%) presumably consists of long, thin microcracks, has a lower flaw density than a strongly heterogeneous, porous (17.5%) carbonate. However, this interpretation is uncertain because Λ is normalized by l_0, an unknown quantity that could take very different values in these two rocks. The only other observation in support of taking large Λ's as an indication of low flaw density is the fact that even larger values of Λ (>1.5) correspond to the two thermally cracked glass samples. Their microstructure, indeed, exclusively consists of cm-scale rather thin and smooth microcracks with intersections distant from each other by a few to tens of millimeters (Mallet et al., 2014).

Even though the absolute values of Λ are practically impossible to interpret, relative variations can be amenable to quantitative analysis. As mentioned earlier, creep experiments at different stress levels were carried in four samples of Etna basalt 1 extracted from the same block and a similar procedure was applied to three samples of Darley Dale sandstone (Heap, 2009). We therefore expect q to be constant in each rock, which is indeed observed for three of the Etna basalt 1 samples ($q = 2$) and all the Darley Dale sandstone ones ($q \approx 7$ or 8). We also note that the inverse of Λ can be expressed as a second-degree polynomial in σ_1

$$\frac{1}{\Lambda} = C_0 - 2C_1\sigma_1 + C_2\sigma_1^2 \tag{13}$$

Indeed, combining Equations 1–3 yields the linear expression, $|\tau_{\text{eff}}| = a\sigma_1 - b$, where the positive constants are given by $a = (1 - \mu)/2$ and $b = \sigma_3 (1 + \mu)/2$. By definition l_0 is proportional to $|\tau_{\text{eff}}|^2 = a^2{\sigma_1}^2 - 2ab\sigma_1 + b^2$ and so is $1/\Lambda = l_0/\lambda$, hence demonstrating Equation 13. The positive constants C_0, C_1, and C_2 are proportional to b^2/λ, ab/λ, and a^2/λ, respectively, and therefore obey the equality $C_2/C_1 = C_1/C_0 = a/b$.

We graphically estimated $\Lambda \approx 0.40$, 1.15, and 1.89 for the three Etna Basalt 1 samples with $\sigma_1/\sigma_{\text{peak}} = 0.97$, 0.86, and 0.80, respectively. Using the values above, the curve of $1/\Lambda$ versus $\sigma_1/\sigma_{\text{peak}}$ is indeed very well fitted with a second-degree polynomial of the same form as in Equation 13. The estimated constants $C_0 = 32.9$, $C_1 = 41.8$, and $C_2 = 53.8$ yield ratios $C_1/C_0 = 1.27$ and $C_2/C_1 = 1.29$ within 1.5% of the theoretical equality. We applied the same analysis to the Darley Dale sandstone data. A value of q greater than 6 was needed, which posed some numerical problems because we had to use a much smaller increment dL of 3×10^{-5} to maintain an acceptable accuracy. Using $q = 8$, we obtained $\Lambda \approx 0.27$, 0.19, and 0.059 for the creep stress levels $\sigma_1/\sigma_{\text{peak}} = 0.84$, 0.88, and 0.93, respectively, which yielded $C_0 = 1{,}560$, $C_1 = 1{,}930$, and $C_2 = 2{,}270$, corresponding to ratios $C_1/C_0 = 1.170$ and $C_2/C_1 = 1.174$ in excellent agreement with the theoretical equality. Thus, the values of Λ fitting the Etna basalt 1 and Darley Dale sandstone experiments are quantitatively consistent with the creep stresses used in them.

3.2. Comparison With Experimental Data: Brittle Failure in Constant Strain Rate Experiments

Since $f(L) = (L/\Lambda)^q$ appears to yield an appropriate description of experimental creep data in a large variety of rocks, it is worth incorporating it in the failure model. Equation 6 thus becomes

$$-1.15\,(|\tau_{\text{eff}}| - \tau_c)\sqrt{\pi a_0\left(1 + \left(\frac{l}{\lambda}\right)^q\right)} + \sigma_3\sqrt{\pi l/2} = 0 \tag{14}$$

Equation 14 can be written in dimensionless form using $\tau^* = (|\tau_{\text{eff}}| - \tau_c)/\sigma_3$, $l^* = l/(1.15^2\, 2a_0)$, and $\lambda^* = \lambda/(1.15^2\, 2a_0)$ (note that the previously used normalization of l and λ to l_0 is not possible here because the remotely applied stresses are not constant in constant strain rate experiments). Solving it for τ^*, yields

$$\tau^* = \sqrt{\frac{l^*}{1 + \left(\frac{l^*}{\lambda^*}\right)^q}} \tag{15}$$

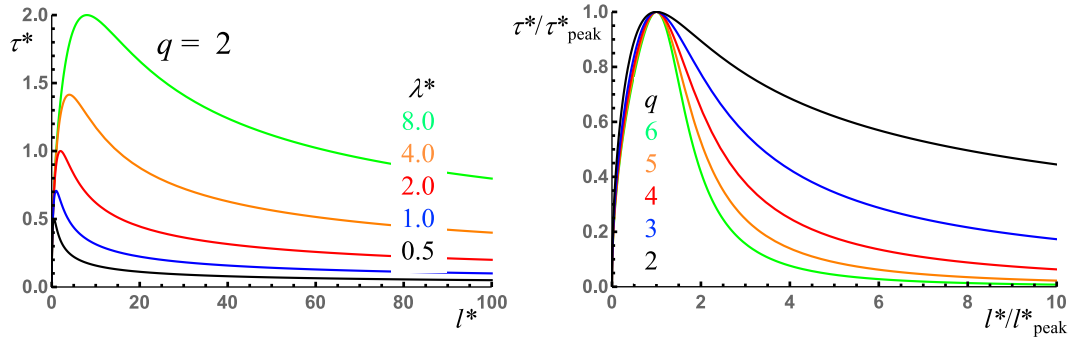

Figure 12. Examples of curves of normalized resolved shear stress τ^* versus normalized wing crack length l^* for the function $(l^*/\lambda^*)^q$ with $q = 2$ and various values of the dimensionless flaw separation λ^* as indicated in matching colors (left diagram). Curves of τ^* versus l^* normalized to their peak values τ^*_{peak} and l^*_{peak}, respectively, for various values of q as indicated in matching colors (right diagram). Importantly, these curves are independent of the values of λ^* used to calculate them (in other words, variations of λ^* at constant q yield exactly coincident curves).

Equation 15 can be used to model constant strain rate tests by calculating the variations of τ^* associated to a constant rate of increase of l^*. We thus determined the τ^* versus l^* curves for q varying from 2 to 12 and λ^* from 0.1 to 16. All curves go through a maximum, $\tau^* = \tau^*_{peak}$, analogous to rock peak strength at $l^* = l^*_{peak}$ (see examples in Figure 12). The right-hand side of Equation 15 is sufficiently simple to allow determining the coordinates of the peak analytically, yielding

$$l^*_{peak} = \lambda^*/(q-1)^{1/q} \tag{16}$$

$$\text{and} \qquad \tau^*_{peak} = \sqrt{\frac{\lambda^*}{q}(q-1)^{\frac{q-1}{q}}}, \tag{17}$$

which implies $\tau^*_{peak} = \sqrt{l^*_{peak}(q-1)/q}$ (see derivation in Appendix B). Thus, l^*_{peak} is proportional to λ^* (the pre-factor decreasing from 1 to ~0.757 and then slightly increasing to ~0.784, when q is increased from 2 to ~4.6 and finally 8). In the same range of q, τ^*_{peak} varies as the square root of λ^* (the pre-factor gradually increasing from ~0.707 to ~0.828). Although the definitions of λ^* and Λ are not identical, these two parameters are both related to the separation distance between microcracks and/or flaws, or in other words, inversely related to the flaw density. As intuitively expected, the model predicts that strength increases with decreasing flaw density (left diagram, Figure 12).

Interestingly, normalizing the shear stress and wing crack length to their values at the peak (i.e., τ^*/τ^*_{peak} and l^*/l^*_{peak}) produced exactly coincident curves for a given value of q, independent of λ^* (right diagram, Figure 12). Thus, λ^* (equivalently, the flaw density) affects the values of τ^*_{peak} and l^*_{peak} but not the shape of the curves. Instead, it is the power law exponent q which appears to control the shape of the τ^* versus l^* curves, particularly the post-peak softening stage. Increasing values of q produce an increasingly sharp softening post-peak behavior (right diagram, Figure 12). Note that, in the softening stage, τ^* asymptotically approaches zero while l^* increases to infinity (Figure 12). This implies that formation of new larger shear bands continues indefinitely at shear stresses ($|\tau_{eff}|$) closer and closer to τ_c, the shear stress, below which wing crack growth was not initially allowed. This property is due to the fact that the model does not include an upper scale limit and therefore does not allow formation of a through-going shear band like those ultimately occurring in (finite size) rock samples deformed to brittle failure.

Stress-strain curves measured in brittle materials are similar to the theoretical curves shown in Figure 12. However, unlike the τ^* versus l^* curves, which represent the results of exclusively inelastic processes, experimental stress-strain curves include both elastic and inelastic strains. For the purpose of comparison with the model, the axial strain, $\varepsilon = \varepsilon_e + \varepsilon_i$, measured in a constant strain rate test must be corrected of its elastic component ε_e so that only the inelastic strain ε_i remains. Elastic strains must obviously be dominant during the early stage of a constant strain rate test when the applied stress is too low to produce significant inelastic deformation. This elastic stage is usually identified as the upwardly curved segment, commonly observed at the beginning of

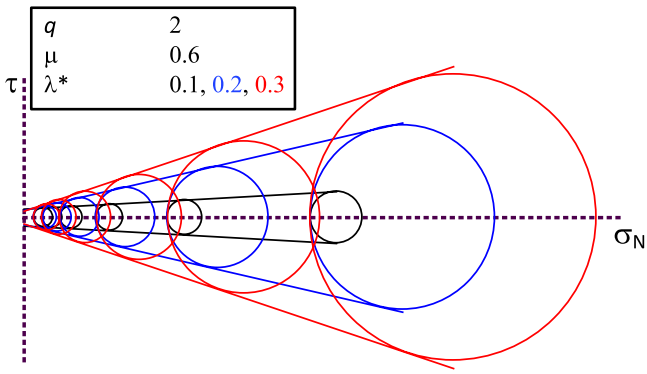

Figure 13. Three examples of Mohr-Coulomb envelope for various values of the model material parameters.

the stress-strain curve (e.g., Heap & Faulkner, 2008). Along this segment, the slope of the stress-strain curve (i.e., the tangent axial Young's modulus E) increases gradually owing to the closure of cracks normal to σ_1 and reaches a maximum at $\sigma_1 = \sigma_c$ that is generally assumed to mark the onset of inelastic deformation. The interpretation of the upwardly curved segment as purely elastic has generally been considered satisfactory in many studies where dilatancy was measured and/or acoustic emissions recorded (among others, Lockner et al., 1992; Lockner, 1993; Stanchits et al., 2006; Fortin et al., 2009; Fortin et al., 2010). However, even if the purely elastic stage of a given laboratory test is accurately identified, determining ε_e along the rest of the stress-strain curve cannot be done without extrapolation unless the elastic properties were actually measured at regular intervals, for example, by running small cyclic stress excursions (e.g., Bernabé et al., 1994). The use of such techniques, however, is extremely rare in practice. Here, we manually digitized the stress-strain curves reported for Etna basalt 1 and Darley Dale sandstone by Heap (2009), since we had previously determined suitable values of q for these rocks, and attempted to construct models of the rocks Young's modulus as a function of stress and total axial strain. Our first attempt yielded values of $(\sigma_{peak} - \sigma_c)/\sigma_3$ (i.e., the equivalent of τ^*_{peak}) that did not scale as the square root of ε_{peak}, the inelastic strain at the peak of the stress-strain curve, as predicted by the model. However, fine-tuning the elastic model brought the results closer to the model prediction. Since the validity of the elasticity models cannot be checked independently, these efforts do not produce truly meaningful results and this approach was not pursued further.

3.3. Correspondence to the Mohr-Coulomb Criterion

Despite decades of intensive work on micromechanical models, the most successful and, therefore, most commonly used brittle failure model is still the simple Mohr-Coulomb criterion, which totally ignores micromechanics. The Mohr-Coulomb criterion states that failure occurs when the Mohr circle corresponding to the state of stress applied to a rock sample becomes tangent to a straight line of equation $t = t_0 + \sigma_N \tan\phi$, where τ_0 is the cohesion and ϕ the internal friction angle. Since only the externally applied principal stresses σ_1 and σ_3 are readily known in triaxial tests, the Mohr-Coulomb criterion is best expressed as (Labuz & Zang, 2012):

$$\tau_m = \sigma_m \sin\phi + \tau_0 \cos\phi, \tag{18}$$

where $\tau_m = 1/2(\sigma_1 - \sigma_3)$ is the radius of the Mohr circle depicting the state of stress at failure and $\sigma_m = 1/2(\sigma_1 + \sigma_3)$ represents the coordinate of the Mohr circle center on the σ_N axis. To check whether or not the Mohr-Coulomb behavior emerges within our model, we need to construct the Mohr circles of failure states predicted by the model for constant values of the material input parameters. Using Equation 17 and the definition of τ^*, we can express the theoretical failure shear stress as

$$\tau_{peak} - \tau_c = \sigma_3 \sqrt{\frac{\lambda^*}{q}(q-1)^{\frac{q-1}{q}}} = \sigma_3 \sqrt{\lambda^* \xi(q)}, \tag{19}$$

which can be recast in terms of the externally applied principal stresses as

$$\sigma_{peak} - \sigma_c = 2\sigma_3 \frac{\sqrt{\lambda^* \xi(q)}}{1-\mu} = \sigma_3 \Psi, \tag{20}$$

where $\sigma_c = 2|K_{Ic}| / \left((1-\mu)1.15\sqrt{\pi a_0}\right)$ is the axial stress corresponding to τ_c. It follows then that $\tau_m = 1/2(\sigma_c + \sigma_3(\Psi - 1))$ and $\sigma_m = 1/2(\sigma_c + \sigma_3(\Psi + 1))$. Plots of Mohr circles calculated for increasing values of σ_3 at constant σ_c, q, and λ^*, indeed, appeared to satisfy the Mohr-Coulomb criterion graphically (Figure 13). This result can also be demonstrated rigorously as follows. We form two independent equations by plugging the above expressions of τ_m and σ_m into Equation 18 for two values of σ_3 differing by an arbitrary factor α (i.e., σ_3 and $\alpha\sigma_3$). Subtracting the first equation from the second, all terms that do not contain σ_3 get removed and we obtain

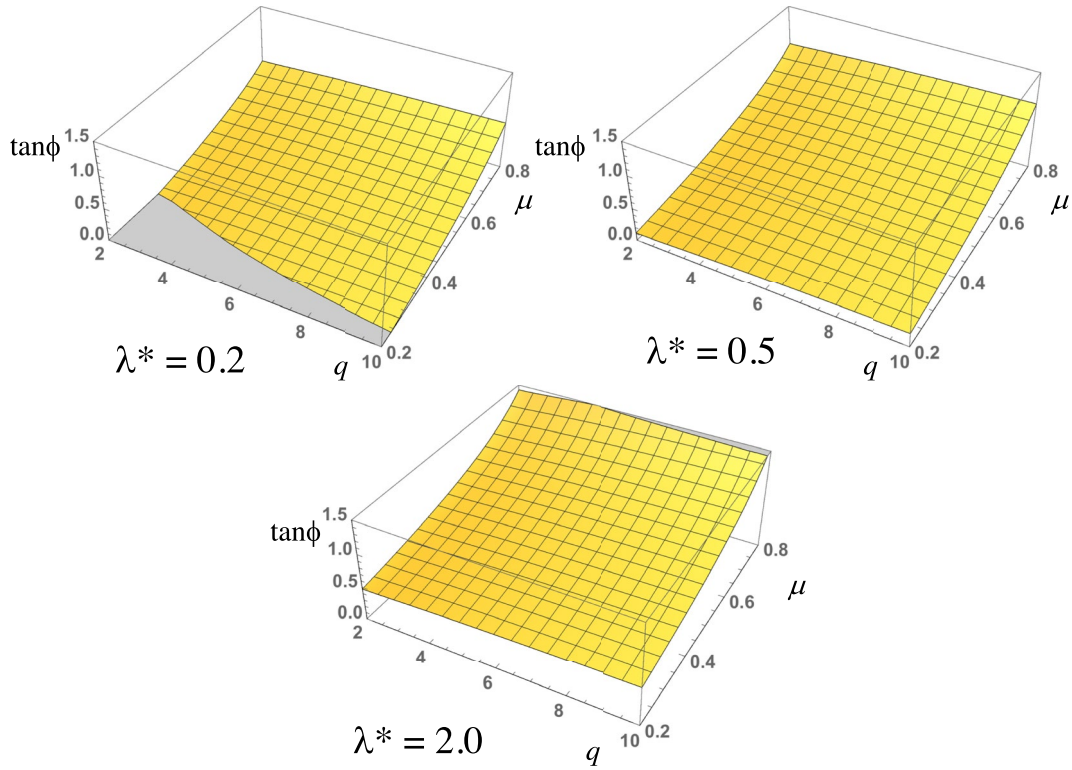

Figure 14. The coefficient of internal friction, tanϕ, as a function of q and μ for three values of the normalized flaw separation λ^*. The gray area in the top-left diagram shows a region where the values of λ^* are below the lower limit λ^*_{min} (see text for more details).

$$\sin\phi = \frac{\Psi - 1}{\Psi + 1}, \tag{21}$$

$$\text{or} \qquad \tan\phi = \frac{\Psi - 1}{2\sqrt{\Psi}}. \tag{22}$$

Returning to the first equation mentioned above, we use Equation 21 to eliminate sinϕ and cosϕ, and after some algebraic manipulations, we obtain

$$\tau_0 = \sigma_c / \left(2\Psi^{1/2}\right). \tag{23}$$

These results demonstrate that the Mohr-Coulomb criterion is recovered from our model because the predicted friction angle and cohesion do not depend on the stress conditions but only on the material constants, σ_c, q, and λ^* (note that, unlike Λ, the normalization factor in λ^* does not contain the principal stresses). Given the remarkably wide applicability of the Mohr-Coulomb criterion to rocks, its emergence in our model is a very important supporting factor and strongly suggests that brittle deformation of rocks is controlled in majority by wing crack growth and related processes. Baud et al. (2014) obtained a similar result using a very different model, albeit one also based on the wing crack model.

We note that Equation 22 predicts an internal friction angle vanishing and becoming negative for $\Psi \leq 1$, indicating that the model yields unphysical results for values of λ^* below a lower limit $\lambda^*_{min} = (1 - \mu)^2/(4\,\xi(q))$. Based on the definition of Ψ, it appears that the modeled internal friction angle is mostly affected by the friction coefficient μ and the normalized flaw separation λ^*, while the exponent q has a rather limited effect. Indeed, the function $\xi(q)$ only increases from 0.5 to 0.72 when q varies from 2 to 10. The coefficient of internal friction, tanϕ, nonlinearly increases with λ^* and μ (Figure 14).

Among the rocks previously discussed in the context of brittle creep, Etna basalt and Darley Dale sandstone were also submitted to a series of dry, constant strain rate tests at different confining pressures (Hackston & Rutter, 2016; Heap, 2009; Zhu et al., 2016). We calculated the failure Mohr circles for each set of experiments and observed that they defined approximately linear envelopes, in good agreement with the Mohr-Coulomb criterion. We then applied Equation 18 to each set of mechanical data to calculate the coefficient of internal friction and the cohesion. From these values and Equations 20, 21 and 23, we computed finally Ψ, σ_c, and λ^* (q is known for both rocks from the previous creep analysis summarized in Figure 11 and values of μ are reported in Baud et al. (2014) and Hackston & Rutter (2016)).

In the case of etna basalt we obtained the following results:			
tanϕ	1.06	0.91	0.91
τ_0 (MPa)	46.4	56.2	45.7
Ψ	6.3	5.1	5.1
σ_c (MPa)	234.	255.	207.
λ^*	3.6	3.3	1.6
	Heap (2009)	(EB_I) Zhu et al. (2016)	(EB_III) Zhu et al. (2016)

The values of tanϕ and τ_0 are somewhat similar to those reported by Baud et al. (2014) for EB_I and EB_III, tanϕ ≈ 0.91 and τ_0 ≈ 46.4 MPa, and tanϕ ≈ 0.81 and τ_0 ≈ 68.0 MPa, respectively. Using Equations 21 and 23, we calculated $\Psi \approx 6.3$ and $\sigma_c \approx 234.$ MPa. The values of λ^* vary from 1.6 to 3.6, with an average of 2.8, indicating a characteristic flaw separation larger than the size of the dominant cracks from which the initial wing cracks emanate. A large flaw separation appears consistent with the microstructure of the intact rocks as revealed from SEM images shown in Zhu et al. (2016). Indeed, the rock consists mainly of a glassy matrix densely speckled with micron-scale inclusions. The glassy matrix also contains few microcracks (most likely the dominant cracks responsible for wing crack formation) and widely separated, large phenocrystals and quasi-spherical vugs (sizes on the order of 200 μm or more). Microcracks are visible inside the phenocrystals but they did not initially extend outside. SEM images of deformed samples reveal very long (several hundred of microns), approximately axially oriented cracks often emanating from (or ending at) vugs but largely avoiding the micron-scale inclusions and phenocrystals (Zhu et al., 2016). It thus appears that these apparent wing cracks were generally able to travel over large distances without clear perturbations, consistent with large values of λ^*. In the case of Darley Dale sandstone the results are:

tanϕ	0.56	0.69
τ_0 (MPa)	25.6	22.2
Ψ	2.9	3.6
σ_c (MPa)	87.	84.
λ^*	0.37	0.58
	Heap (2009)	Hackston and Rutter (2016)

The values of τ_0 obtained here are comparable to 22.1 MPa reported for Wertheim sandstone (a rock with nearly identical porosity and friction coefficient to those of Darley Dale sandstone; Baud et al., 2014). However, tanϕ tends to be slightly smaller than 0.86 observed for Wertheim sandstone. The inferred values of Ψ, σ_c, and especially λ^* appear significantly lower in Darley Dale sandstone than Etna basalt. SEM images of undeformed and deformed Darley Dale sandstone samples, indeed, suggest that grain boundaries were generally partially open and acted as the dominant cracks of the wing crack model (Wu et al., 2000). The characteristic length a_0 is therefore roughly equal to the mean grain size. Although intra-granular cracks are relatively rare in the intact rock, the SEM images reveal the ubiquitous presence of a dense population of asperities along the grain boundaries and irregularities within the inter-granular cement and clays. These defects appear to play an important role in the formation of quasi-axial cracks in samples deformed in the dilatant regime (i.e., at relatively low confining pressures). Under high confining pressures, pore collapse and grain crushing become the prominent deformation mechanisms in porous rocks, implying that our model is not applicable in these conditions. In summary, we found

that, applied to experimental values of the coefficient of internal friction and cohesion of a given rock, our model predicted normalized flaw separations λ^* consistent with the observed microstructure of the rock. The model also infers the onset of inelastic deformation, σ_c, from τ_0. However, the validity of the predicted values of σ_c is hard to assess since (a) the onset of inelastic deformation is not accurately identifiable from stress-strain curves alone (auxiliary techniques such as acoustic emissions monitoring are necessary) and (b) the definition of σ_c involves the critical stress intensity factor κ_{Ic}, a quantity generally unknown in rocks.

4. Implications

We developed a brittle creep and brittle failure model recognizing that flaws in rocks exist over a broad range of length-scales. Our assumption behind the model is motivated by the fact that self-similarity is one of the characteristics of brittle systems; grain size distributions in fault rocks (e.g., Keulen et al., 2007), roughness of frictional interfaces (e.g., Candela et al., 2012), acoustic emissions recorded during experiments (e.g., Goebel et al., 2017), as well as moment-magnitude scaling of crustal earthquakes (Gutenberg & Richter, 1944) are all suggesting that cracking is a process that is self-similar over many orders of magnitude in length scale. The interactions of the dominant microcracks with smaller flaws in their vicinity lead to their coalescence, formation of micro shear bands, and eventually to shear failure when the growing dominant shear band reaches the sample boundaries as typically observed in rocks deformed under confining pressure.

In our model, both the inclined dominant microcracks as well as their associated wing cracks are allowed to grow in contrast to traditional models of brittle creep where only wing crack growth is assumed (e.g., Ashby & Sammis, 1990; Brantut et al., 2012). Comparison of our model to experimental data suggests that the complex and non-tractable interactions of the rock microcracks and flaws can be adequately expressed by the simple power law functions, $f(L) = (L/\Lambda)^q$, where L is the normalized wing crack length and Λ represents the normalized distance over which a wing crack must propagate to interact with other flaws.

The model reproduces all three characteristic stages of creep and returns experimentally determinable quantities, namely the ratio of the time to failure, t_F, to the time of minimum wing crack propagation velocity (i.e., minimum strain rate, or center of the secondary creep segment), t_2, and a power-law exponent, m, that characterizes the mean deceleration rate of primary creep. The model successfully fits data from a broad range of rocks and—with appropriate normalization and accounting for elastic deformation—can be also used to model brittle failure. Furthermore, our model predicts that brittle creep can occur over a very broad range of flaw densities and/or stress levels depending on the exact functional form. Tertiary, accelerating creep has typically been observed only at a high percentage (>50%) of the ultimate failure strength (e.g., Brantut et al., 2012), however recent experiments document primary and secondary brittle creep operating at stress levels as low as ∼10% of the failure strength (Xing et al., 2022) providing evidence that brittle creep indeed occurs over a broad range of stress levels—resolving whether creep at such low fractions of the failure strength will eventually enter the tertiary creep stage is however impossible in the laboratory. As shown in Figure 8, the time to failure predicted by the model varies by over 20 orders of magnitude for the variations of Λ explored in this work.

5. Conclusions

We reformulated the wing crack model of brittle creep and brittle failure to allow for the formation, growth and coalescence of micro shear bands over a broad range of length scales and found that

- The model using a wide class of function $A(L)$ properly returns classical trimodal creep curves for constant stress boundary conditions and characteristic stress-strain curves under constant strain rate boundary conditions
- The model returns dimensionless parameters that can be experimentally measured. Key outputs are the ratio of time to failure, t_F, to the time of minimum strain rate, t_2, and a power-law exponent, m, that characterizes the mean deceleration rate of primary creep. The values of the model input parameters, q and Λ, can then be inferred for each rock considered (see Figure 11).
- The function $A(L) = 1 + f(L)$, where $f(L)$ is a simple power law, $f(L) = (L/\Lambda)^q$, produced values of the constants Λ and q consistent with those estimated from the experimental data. The parameter Λ represents a normalized distance over which a flaw must propagate to interact with other flaws and can be related to flaw density and stress level.

- Polynomial functions which combine the effect of multiple terms with different degrees, yielded results inconsistent with the experimental data, suggesting that brittle creep of rocks can be appropriately described using the power law function, $f(L) = (L/\Lambda)^q$.

Appendix A

The limit Λ_c is the upper limit of Λ such that the curves of $\sqrt{1+(L/\Lambda_c)^q}$ and $\sqrt{L}$ versus L are tangent. As discussed in Section 2.3, the two curves do not intersect when Λ is smaller than Λ_c and they intersect on two separate points for Λ strictly larger than Λ_c. We now note that the curves produced by elevating the two functions above to the power 2 are also tangent to each other for $\Lambda = \Lambda_c$. They therefore have a single common point, where the derivatives of the functions with respect to L must be equal. We can therefore write the two obvious equalities $1 + (L/\Lambda_c)^q = L$ and $q\,(L^{q-1}/\Lambda_c^q) = 1$. Eliminating L between these two equations yields $\Lambda_c = (q^{1/(1-q)} - q^{q/(1-q)})^{(1-q)/q}$.

Appendix B

We wish to calculate the coordinates τ^*_{peak} and l^*_{peak} of the maximum of the curve of τ^* versus l^* predicted by Equation 15. For this, we only need to calculate the derivative with respect to l^* of the right-hand side of Equation 15:

$$\tau'(l^*) = \frac{1 + \left(\frac{l^*}{\lambda^*}\right)^q - q\left(\frac{l^*}{\lambda^*}\right)^q}{2\sqrt{l^*}\left(1 + \left(\frac{l^*}{\lambda^*}\right)^q\right)^{3/2}}$$

Solving $\tau'(l^*) = 0$ for l^* yields the solution $l^*_{\text{peak}} = \lambda^*/(q-1)^{1/q}$ and plugging this value in Equation 15 produces $\tau^*_{\text{peak}} = \sqrt{\frac{\lambda^*}{q}(q-1)^{\frac{q-1}{q}}}$, which can be rewritten $\tau^*_{\text{peak}} = \sqrt{l^*_{\text{peak}}(q-1)/q}$.

Data Availability Statement

Our model is analytical. Computer programming is therefore unnecessary in principle. However, certain parameters such as the power law exponent m are easier to determine numerically. To help interested readers, the Mathematica script used to construct and interpret Figure 8 is available at Zenodo. Except for the Iceland and Etna 2 basalts, we used published experimental data that can be obtained from the articles cited. The Iceland and Etna 2 basalts data were produced in our laboratory and are available at https://doi.org/10.5281/zenodo.6812115.

Acknowledgments
The authors would like to thank Tiange Xing and Elias Mansbach for sharing the data on creep of basalts and Brian Evans for a stimulating and thorough discussion. Funding by MIT Energy Initiative's Carbon Capture, Utilization and Storage Center is gratefully acknowledged. Insightful review by Georg Dresen lead us to explore the connection of our model to the Mohr-Coulomb failure criterion and is gratefully appreciated. Editorial handling by an associate editor and Doug Schmitt is appreciated.

References

Ashby, M. F., & Hallam, S. D. (1986). The failure of brittle solids containing small cracks under compressive stress states. *Acta Metallurgica*, *34*(3), 497–510. https://doi.org/10.1016/0001-6160(86)90086-6

Ashby, M. F., & Sammis, C. G. (1990). The damage mechanics of brittle solids in compression. *PAGEOPH*, *133*(3), 489–521. https://doi.org/10.1007/bf00878002

Baud, P., Reuschlé, T., & Charlez, P. (1996). An improved wing crack model for the deformation and failure of rock in compression. *International Journal of Rock Mechanics and Mining Science & Geomechanics Abstracts*, *33*(5), 539–542. https://doi.org/10.1016/0148-9062(96)00004-6

Baud, P., Wong, T.-F., & Zhu, W. (2014). Effects of porosity and crack density on the compressive strength of rocks. *International Journal of Rock Mechanics and Mining Sciences*, *67*, 202–211. https://doi.org/10.1016/j.ijrmms.2013.08.031

Bernabé, Y., Fryer, D. T., & Shively, R. M. (1994). Experimental observations of the elastic and inelastic behaviour of porous sandstones. *Geophysical Journal International*, *117*(2), 403–418. https://doi.org/10.1111/j.1365-246x.1994.tb03940.x

Brace, W. F., & Bombolakis, E. G. (1963). A note on brittle crack growth in compression. *Journal of Geophysical Research*, *68*(12), 603–614. https://doi.org/10.1029/jz068i012p03709

Brantut, N., Baud, P., Heap, M. J., & Meredith, P. G. (2012). Micromechanics of brittle creep in rocks. *Journal of Geophysical Research: Solid Earth*, *117*(B8), B08412. https://doi.org/10.1029/2012JB009299

Brantut, N., Heap, M. J., Baud, P., & Meredith, P. G. (2014). Mechanisms of time-dependent deformation in porous limestone. *Journal of Geophysical Research: Solid Earth*, *119*(7), 5444–5463. https://doi.org/10.1002/2014JB011186

Brantut, N., Heap, M. J., Meredith, P. G., & Baud, P. (2013). Time-dependent cracking and brittle creep in crustal rocks: A review. *Journal of Structural Geology*, *52*, 17–43. https://doi.org/10.1016/j.jsg.2013.03.007

Candela, T., Renard, F., Klinger, Y., Mair, K., Schmittbuhl, J., & Brodsky, E. E. (2012). Roughness of fault surfaces over nine decades of length scales. *Journal of Geophysical Research*, *117*(B8). https://doi.org/10.1029/2011jb009041

Charles, R. J. (1958). Static fatigue of glass, II. *Journal of Applied Physics*, *29*(11), 1554–1560. https://doi.org/10.1063/1.1722992

Desrues, J. (1990). Shear band initiation in granular materials: Experimentation and theory. In F. Darve (Ed.), *Geomaterials: Constitutive equations and modelling* (pp. 283–310). Elsevier Applied Science.
Desrues, J., & Andó, E. (2015). Strain localization in granular media. *C.R. Physique*, *16*(1), 26–36. https://doi.org/10.1016/j.crhy.2015.01.001
Dieterich, J. H. (2007). Applications of rate-and state-dependent friction to models of fault slip and earthquake occurrence. *Earthquake seismology*, *4*, 107–129.
Fortin, J., Stanchits, S., Dresen, G., & Guéguen, Y. (2009). Acoustic emissions monitoring during inelastic deformation of porous sandstone: Comparison of three modes of deformation. *PAGEOPH*, *166*(5–7), 823–841. https://doi.org/10.1007/s00024-009-0479-0
Fortin, J., Stanchits, S., Vinciguerra, S., & Guéguen, Y. (2010). Influence of thermal and mechanical cracks on permeability and elastic wave velocities in a basalt from Mt. Etna volcano subjected to elevated pressure. *Tectonophysics*, *503*(1–2), 60–74. https://doi.org/10.1016/j.tecto.2010.09.028
Fujii, Y., Kiyama, T., Ishijima, Y., & Kodama, J. (1999). Circumferential strain behavior during creep tests of brittle rocks. *International Journal of Rock Mechanics and Mining Sciences*, *36*(3), 323–337. https://doi.org/10.1016/s0148-9062(99)00024-8
Goebel, T. H. W., Kwiatek, G., Becker, T. W., Brodsky, E. E., & Dresen, G. (2017). What allows seismic events to grow big?: Insights from b-value and fault roughness analysis in laboratory stick-slip experiments. *Geology*, *45*(9), 815–818. https://doi.org/10.1130/G39147.1
Gutenberg, B., & Richter, C. F. (1944). Frequency of earthquakes in California. *Bulletin of the Seismological Society of America*, *34*(4), 185–188. https://doi.org/10.1785/bssa0340040185
Hackston, A., & Rutter, E. (2016). The Mohr-Coulomb criterion for intact rock strength and friction - A re-evaluation and consideration of failure under polyaxial stresses. *Solid Earth*, *7*(2), 493–508. https://doi.org/10.5194/se-7-493-2016
Heap, M. J. (2009). *Creep: Time-dependent brittle deformation in rock* PhD Thesis (p. 399). University.
Heap, M. J., Baud, P., Meredith, P. G., Bell, A. F., & Main, I. G. (2009). Time-dependent brittle creep in Darley Date sandstone. *Journal of Geophysical Research: Solid Earth*, *114*(B7), B07203. https://doi.org/10.1029/2008JB006212
Heap, M. J., Baud, P., Meredith, P. G., Vinciguerra, S., Bell, A. F., & Main, I. G. (2011). Brittle creep in basalt and its application to time-dependent volcano deformation. *Earth and Planetary Science Letters*, *307*(1–2), 71–82. https://doi.org/10.1016/j.epsl.2011.04.035
Heap, M. J., & Faulkner, D. R. (2008). Quantifying the evolution of static elastic properties as crystalline rock approaches failure. *International Journal of Rock Mechanics and Mining Sciences*, *45*(4), 564–573. https://doi.org/10.1016/j.ijrmms.2007.07.018
Horii, H., & Nemat-Nasser, S. (1985). Compression-induced microcrack growth in brittle solids: Axial splitting and shear failure. *Journal of Geophysical Research*, *90*(B4), 3105–3125. https://doi.org/10.1029/jb090ib04p03105
Kachanov, M. L. (1982). A microcrack model of rock inelasticity. Part II: Propagation of microcracks. *Mechanics of Materials*, *1*, 29–41. https://doi.org/10.1016/0167-6636(82)90022-9
Keulen, N., Heilbronner, R., Stünitz, H., Boullier, A.-M., & Ito, H. (2007). Grain size distributions of fault rocks: A comparison between experimentally and naturally deformed granitoids. *Journal of Structural Geology*, *29*(8), 1282–1300. https://doi.org/10.1016/j.jsg.2007.04.003
Labuz, J. F., & Zang, A. (2012). Mohr-Coulomb failure criterion. *Rock Mechanics and Rock Engineering*, *45*(6), 975–979. https://doi.org/10.1007/s00603-012-0281-7
Lajtai, E. Z. (1974). Brittle fracture in compression. *International Journal of Fracture*, *10*(4), 525–536. https://doi.org/10.1007/bf00155255
Lin, Q. B., Cao, P., Wen, G. P., Meng, J. J., Cao, R. H., & Zhao, Z. Y. (2021). Crack coalescence in rock-like specimens with two dissimilar layers and pre-existing double parallel joints under uniaxial compression. *International Journal of Rock Mechanics and Mining Sciences*, *139*, 104621. https://doi.org/10.1016/j.ijrmms.2021.104621
Lockner, D. A. (1993). The role of acoustic emissions in the study of rock fracture. *International Journal of Rock Mechanics and Mining Science & Geomechanics Abstracts*, *30*(7), 883–899. https://doi.org/10.1016/0148-9062(93)90041-b
Lockner, D. A. (1998). A generalized law for brittle deformation of Westerly granite. *Journal of Geophysical Research*, *103*(B3), 5107–5123. https://doi.org/10.1029/97jb03211
Lockner, D. A., Byerlee, J. D., Kuksenko, V., Ponomarev, A., & Sidorin, A. (1992). Observations of quasistatic fault growth from acoustic emissions. In B. Evans & T.-F. Wong (Eds.), *Fault mechanics and transport properties of rocks* (pp. 3–31). Academic Press.
Main, I. G. (2000). A damage mechanics model for power-law creep and earthquake aftershock and foreshock sequences. *Geophysical Journal International*, *142*(1), 151–161. https://doi.org/10.1046/j.1365-246x.2000.00136.x
Mallet, C., Fortin, J., Guéguen, Y., & Bouyer, F. (2014). Evolution of the crack network in glass samples submitted to brittle creep conditions. *International Journal of Fracture*, *190*(1–2), 111–124. https://doi.org/10.1007/s10704-014-9978-9
Mallet, C., Fortin, J., Guéguen, Y., & Bouyer, F. (2015). Brittle creep and subcritical crack propagation in glass submitted to triaxial conditions. *Journal of Geophysical Research: Solid Earth*, *120*(2), 879–893. https://doi.org/10.1002/2014JB011231
Mansbach, E. (2022). Effect of Carbon sequestration and reservoir conditions on brittle creep in Etna basalt. *Thesis Commons*. https://doi.org/10.31237/osf.io/64gxc
Marone, C. (1998). Laboratory-derived friction laws and their application to seismic faulting. *Annual Review of Earth and Planetary Sciences*, *26*(1), 643–696. https://doi.org/10.1146/annurev.earth.26.1.643
Paterson, M. S., & Wong, T.-F. (2005). *Experimental rock deformation - the brittle field* (2nd ed., p. 347). Springer.
Rawling, G. C., Baud, P., & Wong, T.-F. (2002). Dilatancy, brittle strength, and anisotropy of foliated rocks: Experimental deformation and micromechanical modeling. *Journal of Geophysical Research: Solid Earth*, *107*(B10), ETG 8-14. https://doi.org/10.1029/2001JB000472
Stanchits, S., Vinciguerra, S., & Dresen, G. (2006). Ultrasonic velocities, acoustic emission characteristics and crack damage of basalt and granite. *PAGEOPH*, *163*(5–6), 974–993. https://doi.org/10.1007/s00024-006-0059-5
Wiederhorn, S. M., & Bolz, L. H. (1970). Stress corrosion and static fatigue of glass. *Journal of the American Ceramic Society*, *53*(10), 543–548. https://doi.org/10.1111/j.1151-2916.1970.tb15962.x
Wong, N. Y. (2008). *Crack coalescence in molded gypsum and Carrara marble* PhD Thesis (p. 876). MIT.
Wong, N. Y., & Einstein, H. H. (2009a). Crack coalescence in molded gypsum and Carrara marble: Part 1- Macroscopic observations and interpretations. *Rock Mechanics and Rock Engineering*, *42*(3), 475–511. https://doi.org/10.1007/s00603-008-0002-4
Wong, N. Y., & Einstein, H. H. (2009b). Crack coalescence in molded gypsum and Carrara marble: Part 2- Microscopic observations and interpretation. *Rock Mechanics and Rock Engineering*, *42*(3), 513–545. https://doi.org/10.1007/s00603-008-0003-3
Wu, X. Y., Baud, P., & Wong, T.-F. (2000). Micromechanics of compressive failure and spatial evolution of anisotropic damage in Darley Dale sandstone. *International Journal of Rock Mechanics and Mining Sciences*, *37*(1–2), 143–160. https://doi.org/10.1016/s1365-1609(99)00093-3
Xing, T., Ghaffari, H. O., Mok, U., & Pec, M. (2022). Creep of CarbFix basalt: Influence of rock-fluid interaction. *Solid Earth*, *13*(1), 137–160. https://doi.org/10.5194/se-13-137-2022
Zhu, W., Baud, P., Vinciguerra, S., & Wong, T.-F. (2016). Micromechanics of brittle faulting and cataclastic flow in Mount Etna basalt. *Journal of Geophysical Research: Solid Earth*, *121*(6), 4268–4289. https://doi.org/10.1002/2016JB012826
Zoback, M. L., & Zoback, M. (2007). Lithosphere stress and deformation. In G. Schubert (Ed.), *Treatise on geophysics* (2nd ed., pp. 255–271). Elsevier. https://doi.org/10.1016/B978-0-444-53802-4.00115-9